JOURNAL OF MATERIALS SCIENCE 31 (1996) 6409–6422

Volume change and light scattering during mechanical damage in polymethylmethacrylate toughened with core–shell rubber particles

R. SCHIRRER, C. FOND, A. LOBBRECHT
Institut Charles Sadron, 6 rue Boussingault, F-67083 Strasbourg, France

Mechanical damage was investigated in polymethylmethacrylate toughened with core–shell (hard core) rubber particles. During a tensile experiment, volume changes, light absorption, light scattering and a small strain elastic modulus were recorded. Light scattering was quantitatively related to the number of damaged particles and a fast partial unloading technique allowed determination of the non-elastic part of these changes in material properties. Experiments performed between 10^{-5} and $10^{-1}\,s^{-1}$ and between 20 and 70 °C showed time–temperature transitions. These appeared to be different for each property, and measurement of the activation energy for each parameter enabled microscopic damage mechanisms to be inferred. Three types of microstructural damage were observed: pure matrix plasticity at very low strain rates or high temperatures, rubber cavitation at correlated locations at medium strain rates and temperatures, and disordered cavitation, rubber tearing and matrix plasticity at high strain rates or low temperatures. The experimental mean stress triggering rubber cavitation was compared with the predicted value.

1. Introduction

Glassy polymers are mainly rather brittle materials and if used for structural applications, are modified to behave in a more ductile manner and to develop large damage zones before breakage. The techniques employed to toughen such polymers vary depending on the nature of the material. Inclusion of small rubber particles in the glassy polymer matrix is one very common way of achieving a high degree of toughness. The particles may consist of pure rubber, or may have an inner structure as in the so-called "core–shell", "onion" or "salami" particles. Toughening mechanisms in this type of polymer blend have given rise to a large number of experimental studies in many different polymers [1–4]. In PMMA, these studies have shown that yielding on a local scale could be the main deformation mechanism, and the best toughening is obtained for a specific structure and size of the rubber particle. More recently, it has been experimentally demonstrated in several materials, that rubber particles cavitate and that this cavitation may be the precursor triggering the other damage mechanisms [5–10]. A first theoretical analysis of cavitation in pure rubber [11–13] showed that particles may cavitate even under low mean tensile strain. A more refined model has now been proposed, discussing the nature and the mechanism of onset of the void and including a volume conservation criterion [14]. On the other hand, core–shell particles are preferred to pure rubber particles in many industrial polymers and although some experimental work on this type of material has been done [16], a theoretical analysis of core–shell toughening has still to be performed. Experimentally, changes in microstructure during a tensile process may be followed by many techniques including volume change [1, 16], light transmission [16, 17, 18], X-ray diffraction [8], and post-mortem microscopy.

In this paper, the mechanical definition of damage (a decrease in modulus) was used to characterize changes in the inner structure of rubber-toughened polymethylmethacrylate (RT-PMMA) during the deformation process. Unrecoverable volume changes, Poisson's ratio, lost energy and light transmission and scattering were recorded simultaneously. Techniques of measurement were developed to allow experiments over wide ranges of strain rate (10^{-5}–$10^{-1}\,s^{-1}$) and temperature (20–70 °C). A partial fast unloading technique was used to estimate the non-elastic volume change, while light transmission was found to be quantitatively related to the number of damaged rubber particles. Time–temperature transitions were carefully examined and experimental results compared with predicted values.

2. Experimental procedure

2.1. Material

The polymer was a low molecular weight PMMA ($M_w = 120\,000$) containing 40% core–shell rubber particles, referred to as Altuglas El-CH 60 (Atohaas Company). In this material, the particles have a hard core (PMMA), a cross-linked rubbery shell (butylacrylate-styrene) and an outer PMMA shell; the

0022–2461

particle diameter is about 200 nm and the rubber content is 15 wt % total. Refractive index of the particles is matched to that of the matrix in order to obtain transparency. The normalized tensile modulus is approximately 1900 MPa and the Charpy toughness 60 kJ m^{-2}. As will be seen later, this material is particularly convenient for study, because the transitions of the main mechanical properties (brittle–ductile, volume changes, plasticity or damage, ...) arise in the usual experimental ranges of temperature and strain rate (20–60 °C and 10^{-5}–10^{-1} s^{-1}). Fig. 1 shows the structure of the polymer blend.

2.2. Mechanical measurements

As shown in Fig. 2, the sample was a simple tensile sample, about 100 mm long, 10 mm wide and 2 mm thick of strictly constant cross-section along its entire length in order to ensure homogeneous damage. The cross-section was recorded by means of a transverse strain gauge, ε_y, and the longitudinal strain was recorded with an identical strain gauge. Volume changes were calculated using the simple equation for small strains

$$\Delta V/V = \varepsilon_x + 2\varepsilon_y \quad (1)$$

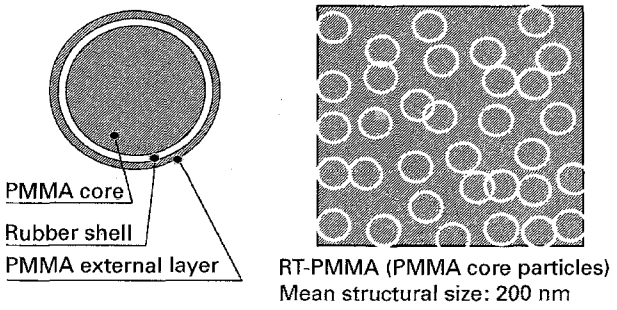

Figure 1 Rubber toughened PMMA containing toughening particles with a hard core (PMMA) and a rubbery shell. The particle diameter is 200 nm, the particle content is about 40% and the rubber represents only a few per cent of the overall material.

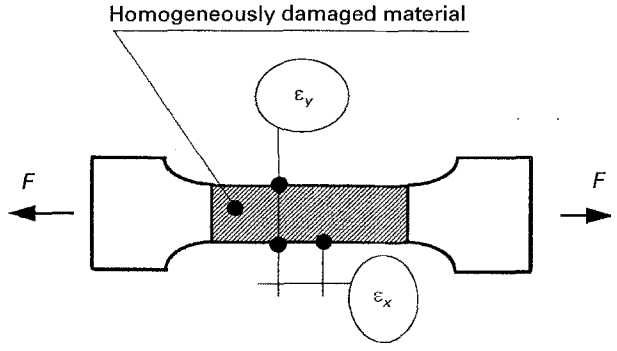

Figure 2 RT-PMMA for tensile experiments, a standard tensile sample about 100 mm long, 10 mm wide, 2 mm thick. The damage zone must be homogeneous to allow valid measurements. Two "clip-on" strain gauges are fitted on the sample to measure the changes in cross-section during deformation.

An important requirement of this relation is that the deformation must be rigorously homogeneous in the volume located between the strain gauge pins.

The sample was tested with an Instron hydraulic tensile machine (crosshead speed up to 600 mm s^{-1}), using a special software generating a constant crosshead speed with 30 equally spaced small unloadings at constant high speed. The temperature in the environmental chamber could be controlled with 1 °C accuracy from room temperature to above the glass transition temperature of the polymer.

One possible damage parameter, D, is defined by the tensile modulus, E, calculated from small unloadings according to the usual formula

$$D = 1 - E/E_0 \quad (2)$$

In the case of highly viscoelastic polymers, the small unloadings must be applied at a strain rate at least one decade above the main loading strain rate. Indeed, if an unloading is applied at the same strain rate as the load, a hysteretic loop appears during the unloading and relaxation occurs, as shown in Fig. 3. A decrease in the purely viscous modulus could then be interpreted as a damage process. In the measurements illustrated in Fig. 4, where the unloading strain rate was constant and equal to 0.5 s^{-1}, the last unloading shows that the remaining true strain, ε_{pl}, after full unloading (the "non-recoverable" or "plastic" true strain), may be obtained by linear extrapolation of the small unloadings. In fact, ε_{pl} is time dependent in polymers and may partially recover with time, especially at high temperatures. ε_{pl} could also be defined as the total strain less the instantaneous elastic strain.

The damage as depicted in Fig. 5, generally exhibits an increase within the first 10% strain, during the onset of plasticity. At higher strains, molecular orientation increases the tensile modulus in the tensile direction and the material becomes strongly

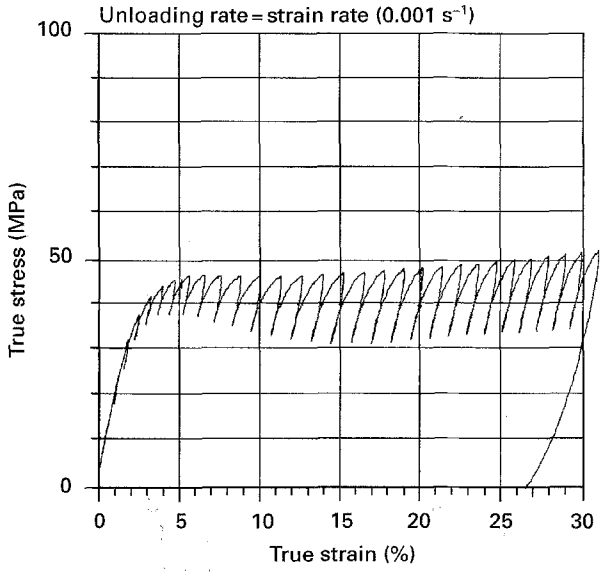

Figure 3 True stress versus true strain with small unloadings at the same strain rate as the loading rate. A large hysteretic response appears during each unloading, leading to a meaningless damage measurement.

anisotropic. The decrease in modulus due to damage is thus partially or even fully compensated by anisotropy.

Correction for the elastic part is particularly important for volume changes (Fig. 6). The total volume change is always positive, (including the elastic volume change as Poisson's ratio is lower than 0.5), showing small "ticks" at each unloading. Using these ticks extrapolated as on Fig. 4 it is possible to calculate the elastic part of the volume change. The remaining non-elastic volume change is almost zero during first damage (0%–7% strain), and subsequently increases steadily. Therefore, a limiting value, $\varepsilon_{v=0}$, may be defined and its changes with temperature and strain rate investigated. As shown in Fig. 7, Poisson's ratio remains almost constant during the damage process, in the range 0.3–0.35 as expected at small strain for glassy polymers.

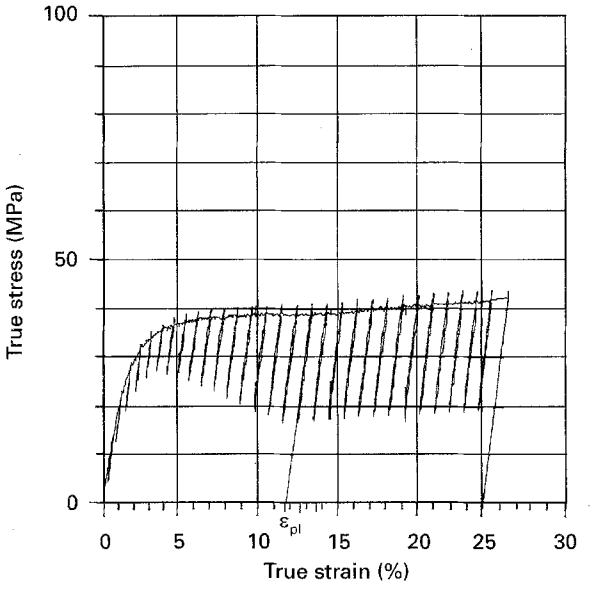

Figure 4 True stress–strain curve at 20 °C, and 10^{-3} s^{-1} strain rate. The small unloadings are applied at high strain rate (0.5 s^{-1}), leading to linear unloadings. The curve exhibits a classical elastic–plastic shape. "Damage", D, may be calculated from the unloading modulus.

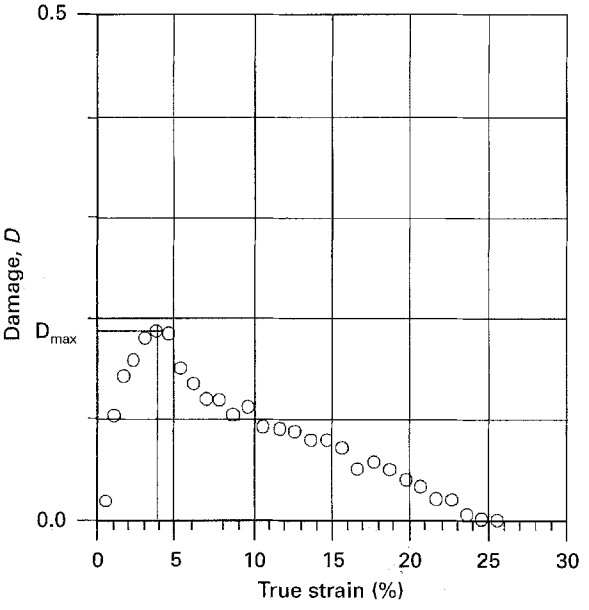

Figure 5 Damage as defined by the modulus of the material during the small unloadings. The apparent decrease in damage is due to molecular orientation at high strains, which induces a stiffening of the material at 20 °C, and strain rate 10^{-3} s^{-1}.

2.3. Optical measurements

A mechanical definition of damage does not provide any information about its nature at the microscopic level. There exist many methods to obtain microstructural information, for instance X-ray scattering, light scattering, ultrasonic measurements and electron microscopy. In this study, as the polymer was transparent, and became white during damage, the simplest

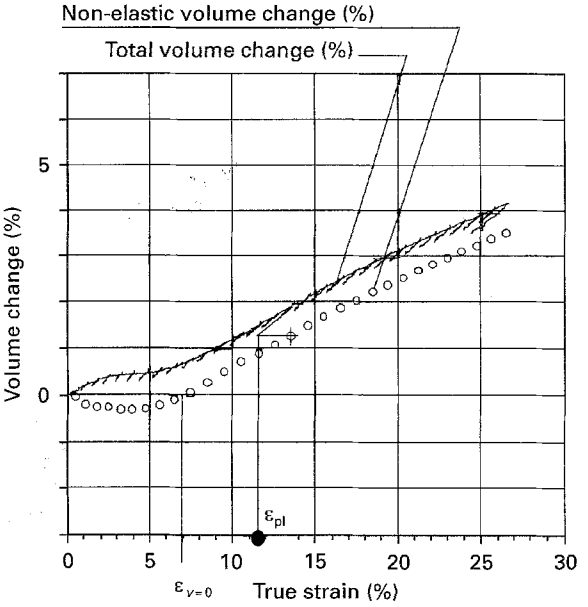

Figure 6 The total volume change is the elastic volume change, Poisson's ratio being lower than 0.5 and the volume change due to the damage process. The volume change, less the elastic part, is almost zero during the first damage (0%–7% strain), and then increases steadily (20 °C, strain rate 10^{-3} s^{-1}).

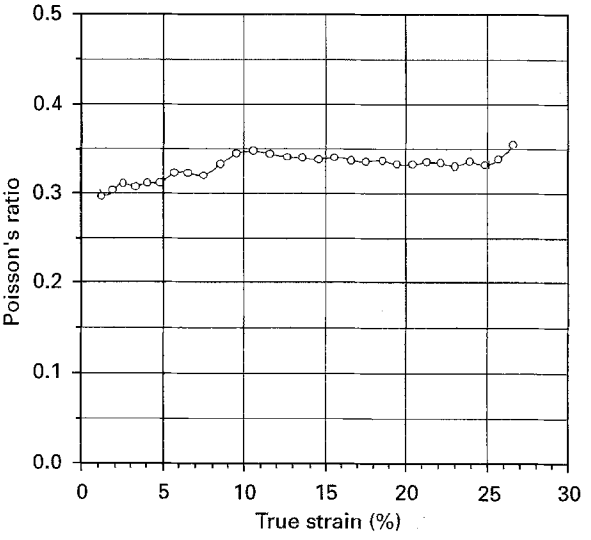

Figure 7 Poisson's ratio remains almost constant during the damage process, in the range 0.3–0.35 as expected for glassy polymer at small strain (20 °C, strain rate 10^{-3} s^{-1}).

procedure was the simultaneous measurement of light scattering at the beginning of the damage and light absorption at high strain and damage, when multiple scattering occurred (Fig. 8). A first attempt to estimate cavitation in rubber particles employed light back-scattering [17, 18]. The experimental system shown here was designed to combine scattering and absorption measurement with a semi-quantitative interpretation. A laser beam was used to produce the light scattering pattern and simultaneously determine the light transmission, the area investigated by the beam being small (1 mm^2) and located close to the strain gauges in order to provide good correlation between the mechanical and optical measurements. The response of the light converter was linear over at least five decades, and the band width of the recorder greater than 1 kHz. Unfortunately, the CCD camera was a standard apparatus giving only 25 pictures s^{-1}. At the highest strain rates applied (0.1 s^{-1}), the light transmission recording was, therefore, still clean, but the light diffusion pattern sometimes changed sharply from one picture frame to the next.

If one assumes each damaged site to behave as a small light scatterer of less than 200 nm size, total light absorption may be estimated as a function of the density of the damaged sites (see Appendix 1)

$$\log(I/I_0) \approx -Tv_p d^{-1} \phi\xi \log(e) \qquad (3)$$

where ϕ is the fraction (in number) of damaged particles, ξ the scattering cross-section of a damaged particle (unknown), v_p the volume fraction of the particles, d the particle diameter, T the sample thickness, and $e = 2.7182$. The fraction of damaged particles, ϕ, is then directly proportional to the light transmission. Because the product $\phi\xi$ cannot be dissociated, the decrease in light intensity is proportional either to the number of damaged sites or to their size. In the case of the polymer sample of this study, the numerical factors take the following value

$$\phi\xi \approx -0.58 \times 10^{-3} \log(I/I_0) \qquad (4)$$

Experimental light intensities were recorded on a log scale, as in the typical example of Fig. 9. Equation 4 also shows that even for a degree of damage at which the light absorption is as high as two decades ($\log(I/I_0) = -2$), the density of damaged sites is still low, ($\phi\xi \approx 10^{-3}$), with only 1 in 1000 of the particles damaged, for $\xi = 1$. At this level of damage, the mean distance between damaged particles is about ten times ($1000^{1/3}$) the mean distance between particles, in the present case being 2.7 μm.

The diffraction pattern of Fig. 10 indicates that the damaged sites are not randomly distributed throughout the material, but located in organized layers, which points to the existence of particle interaction. On this image, the angle between the strain direction and the cross is about 35°. Light scattering would therefore appear to be much more sensitive than light absorption to detect first damage. The angle at which plasticity develops in the matrix around a ruined particle depends on the material properties [13] and the ruined particles align along "dilatational bands" or "croids" [10], located on a cone (angle α) around the stress direction (Fig. 11). Because the light beam is perpendicular to the stress direction, the diffraction pattern integrates the diffraction from dilatational bands having apparent projection angles ranging from 0–α. Hence the diffraction pattern never shows two thin bright lines, but rather the broad cross-shaped area of Fig. 10. Although the theoretical angle is of the

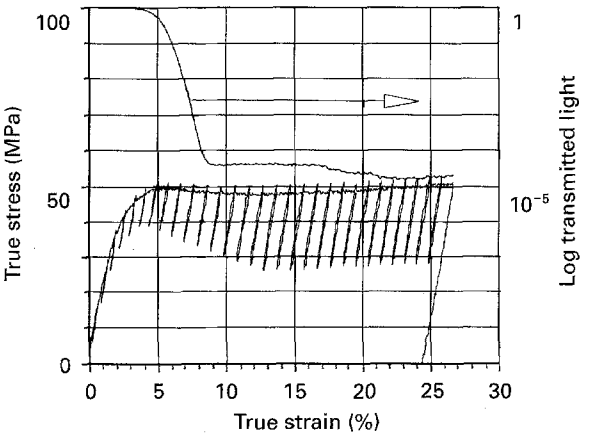

Figure 9 Light absorption versus strain (20 °C, strain rate 10^{-3} s^{-1}). The constant light transmission at about 10^{-4} represents the noise level.

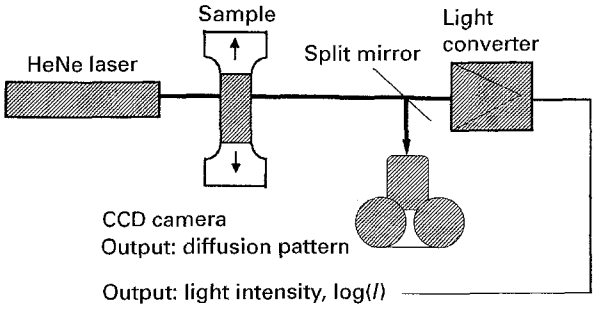

Figure 8 During the deformation process, a HeNe laser beam was used to measure light absorption (light converter) and light scattering (CCD camera).

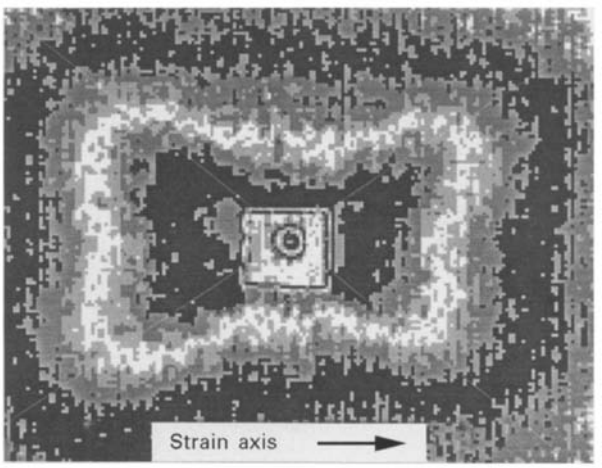

Figure 10 Light diffraction gives a cross-like pattern, the strain direction being horizontal on the figure (20 °C, 5% strain, strain rate 10^{-3} s^{-1}).

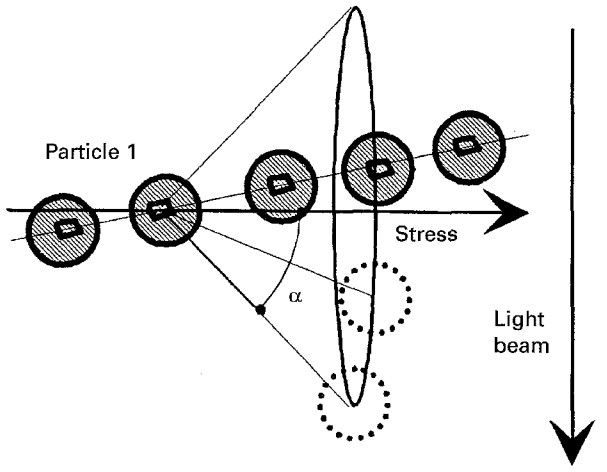

Figure 11 The dilatational band, starting from the cavitated particle 1, is located anywhere on a cone having an angle α with the stress direction.

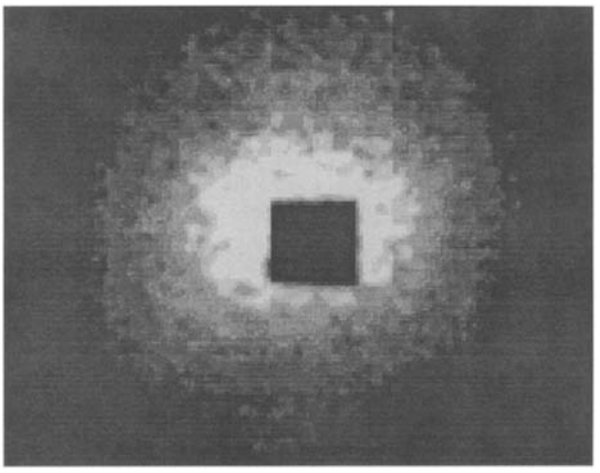

Figure 12 At high level of damage, when light absorption is greater than a factor of 10, the diffraction pattern is blurred by multiple scattering (20 °C, 8% strain, strain rate $10^{-3}\,s^{-1}$).

same order as the experimental value found here, the broadness of the cross strongly limits the quantitative interpretation of the diffraction pattern [19].

At high strain (above 10%) and low temperature, multiple light scattering occurs and the scattering pattern becomes blurred as shown in Fig. 12. Light absorption is then the better parameter to measure. This parameter indicates how the damaged sites density increases with strain, a property which, like any characteristic of a polymeric material, depends strongly on temperature and strain rate. In summary, light scattering gives precise indication of the onset and organization of early particle cavitation, whereas light absorption gives a quantitative measure of particle cavitation at high levels of damage.

3. Results as a function of strain rate and temperature

3.1. Damage *D*

The highest value D_{max} of the damage D as defined in Fig. 5 is reached at a strain ε_{Dmax} which shows less than 10% dependence on strain rate, and only weakly

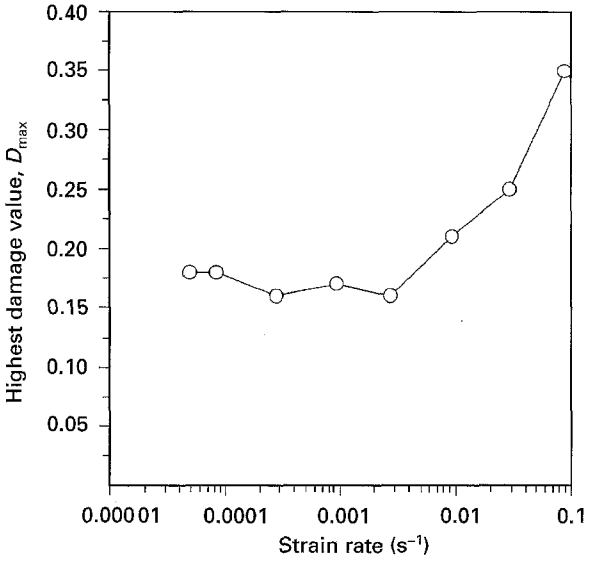

Figure 13 Highest level of the damage, D_{max}, as defined in Fig. 5, versus strain rate at 20 °C.

increases with rate. As mentioned previously, strain hardening due to molecular orientation seems efficiently to compensate for the effect of the damage on the modulus. D_{max} itself depends strongly on strain rate and temperature, an expected result for any mechanical property of a polymer. As shown in Fig. 13, the damage at low rates is small, corresponding mainly to the development of plasticity, whereas the damage at higher rates or lower temperatures is greater, corresponding first to destruction of the microstructure and subsequently to the onset of plasticity. However, D_{max} is somewhat difficult to define with precision. Owing to large scatter in the values of D_{max} and the strain at which it occurs, no attempt was made to define a more precise correlation between this parameter and experimental factors. Volume changes, light absorption and the diffraction pattern are, in fact, much more sensitive to experimental conditions.

3.2. Volume change

3.2.1. General behaviour

Our investigation concerned the volume change corrected for the elastic volume change as defined earlier. The threshold strain, $\varepsilon_{v=0}$, below which the volume remains constant (Fig. 6) depends on strain rate and temperature (Fig. 14). At low strain rates, the volume remains constant for any strain or level of damage. Above the critical rate, the volume increases with strain above $\varepsilon_{v=0}$ with a slope also increasing with strain rate and can reach up to 50% of the theoretical increase in the case of a purely dilatational strain (Poisson's ratio = 0). Fig. 15 summarizes the situation and defines a limiting strain rate $(d\varepsilon/dt)_{max}$ of about $10^{-3}\,s^{-1}$ at 20 °C below which the volume remains constant during the entire deformation.

3.2.2. Activation energy of the volume change

Because the limiting rate $(d\varepsilon/dt)_{max}$ varies with temperature, an activation energy can be inferred from the

time–temperature master curve. Fig. 16 shows that the mechanism follows an Arrhenius law with an activation energy of about 12 kcal mol^{-1}, while the activation energy for mechanical properties of the type of rubber used in the core–shell particles is of the order of 10 kcal mol^{-1}. Hence the value found for the volume increase is consistent with a mechanism involving fracture in the rubber shell of the particles.

3.3. Energy dissipated during damage

The energy dissipated during the course of damage corrected for the elastic contribution, is plotted in Fig. 17 as a function of strain rate, for the level of damage at which the light transmission is decreased by four decades, a situation corresponding at first glance to a constant high number of damaged sites. At high strain rates, the material is brittle, and requires four to five times less energy than at low rates. This result is consistent with the previous finding of greater values of D_{max} at high strain rates (Fig. 13). As might be expected, extensive rubber cavitation followed by rubber rupture with volume increase, consumes less energy than minor cavitation and subsequent shearing without volume increase.

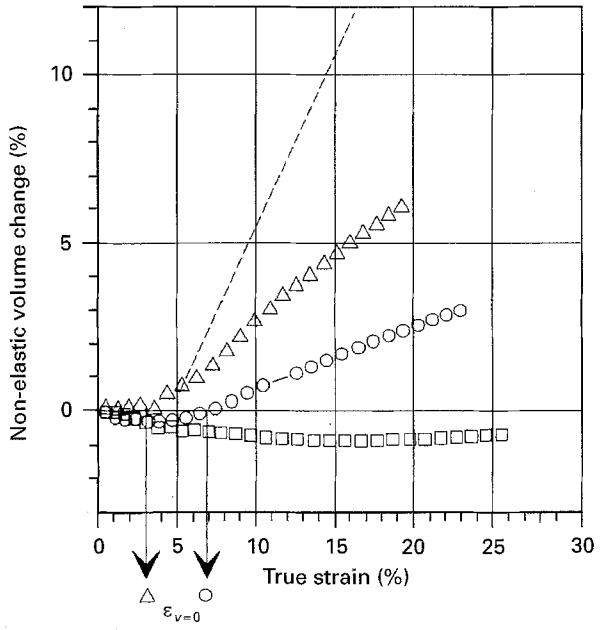

Figure 14 Volume change corrected for elastic changes, at 20 °C and 3 different strain rates: (Δ) 3×10^{-2} s^{-1}, (○) 10^{-3} s^{-1}, and (□) 5×10^{-5} s^{-1}. Below the limiting rate $(d\varepsilon/dt)_{max}$, the volume remains unchanged, while the dashed line (slope = 1) represents the volume increase for a purely dilatational uniaxial strain ($\nu = 0$).

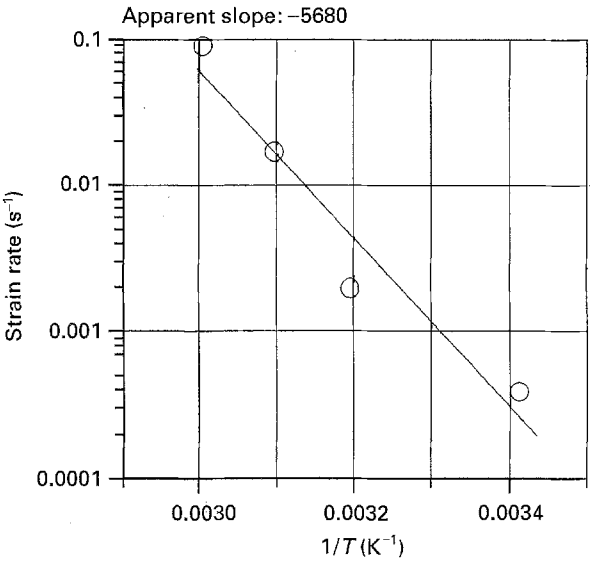

Figure 16 Arrhenius plot of the limiting strain rate $(d\varepsilon/dt)_{max}$ below which the volume remains constant during the entire damage process. The slope corresponds to an apparent activation energy of 12 kcal mol^{-1}.

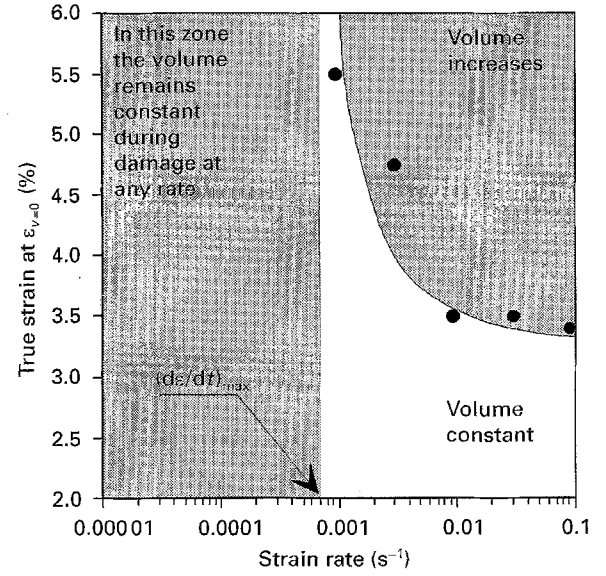

Figure 15 Threshold strain, $\varepsilon_{v=0}$, below which the volume remains constant during the entire damage process, plotted as a function of strain rate at 20 °C.

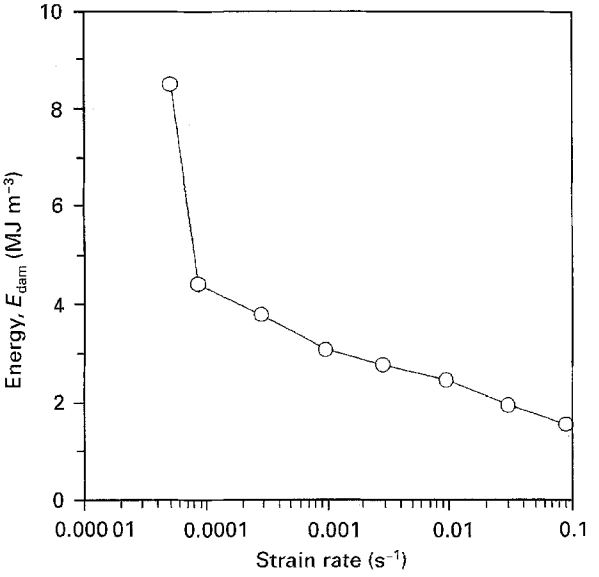

Figure 17 The energy dissipated at 20 °C at a level of damage corresponding to four decades of light absorption decreases at high strain rates.

3.4. Light absorption and scattering

3.4.1. General behaviour

Once the light diffraction patterns shown in Figs 10 and 12 have appeared, there is little further change in light scattering with strain rate and temperature. The angle of the cross would be expected to change slightly, but the broadness of the pattern is too large to allow precise measurements. However, the critical value of strain at which the cross appears and the strain at which the cross merges into a bright circular spot due to multiple diffusion, depend strongly on strain rate and temperature. At high temperatures and low strain rates, the material remains transparent at any stage of deformation. At intermediate temperatures and strain rates, the diffraction cross appears below 5% strain and its intensity increases steadily throughout the deformation process. The cross branches are then not too broad, indicating a relatively good spatial correlation of the dilatational bands. At high strain rates or low temperatures, although the diffraction cross still appears below 5% strain, it is broad and soon transforms (at 6% or 7% strain) into the circular spot characteristic of multiple diffusion.

The onset of particle cavitation may be more quantitatively examined by light absorption. Fig. 18 presents the results at 50 °C for three strain rates, chosen close to the transition from a low level of cavitation where the material is still almost transparent, to a high cavitation density where the material becomes strongly light absorbing. The tensile modulus does not vary greatly within these two decades of strain rate (1655–1788 MPa), but the yield stress of the material shows an important change (30–50 MPa). At highest cavitation density, the stress–strain curve shows a small degree of strain softening at 5% strain, as the level of cavitation increases rapidly with strain.

Fig. 19 depicts the relationships between volume change, cavitation density according to the light absorption and dissipation of mechanical energy. This energy was corrected for the elastic part by subtracting from total energy, the instantaneously recoverable elastic energy (Fig. 4). If one considers a given level of cavitation density, for instance four decades of light absorption, the process of cavitation may be seen to be more energy consuming at low than at high strain rates, with a five-fold difference for three decades of strain rate. In all cases, cavitation occurs without measurable volume change and volume increases seem to arise at a later stage of the particles destruction. At onset, the cavity diameter is very small compared to the particle diameter (less than 10%), leading to less than 10^{-3} volume change [14].

3.4.2. Light absorption activation energy

As the light absorption due to particle cavitation depends strongly on time and temperature, its detailed time and temperature behaviour was investigated. The most difficult point was to decide the level of light absorption below which the material could be considered to remain transparent and the threshold absorption of about half a decade at 15% strain, was chosen to lie in a range where light measurements are still precise. Fig. 20 shows experimental results for three different sets of time and temperature conditions under which the light absorption is almost identical (70 °C and $3 \times 10^{-2}\ s^{-1}$, 60 °C and $2.9 \times 10^{-3}\ s^{-1}$, 50 °C and $3.2 \times 10^{-4}\ s^{-1}$). Surprisingly, the stress–strain curves in these three situations are rigorously the same, whereas the tensile moduli are not (1390, 1580 and 1655 MPa). Thus, the yielding behaviour of the material would appear to be closely linked to the particles' cavitation.

When examined on an Arrhenius plot (Fig. 21), the onset of light absorption and hence of cavitation may be seen to follow a linear law with an activation energy of about 22 kcal mol^{-1}, equal to the activation energy for plastic flow below the glass transition of pure PMMA. This confirms the dominant role of the plasticity of the matrix in the mechanism of the particle cavitation.

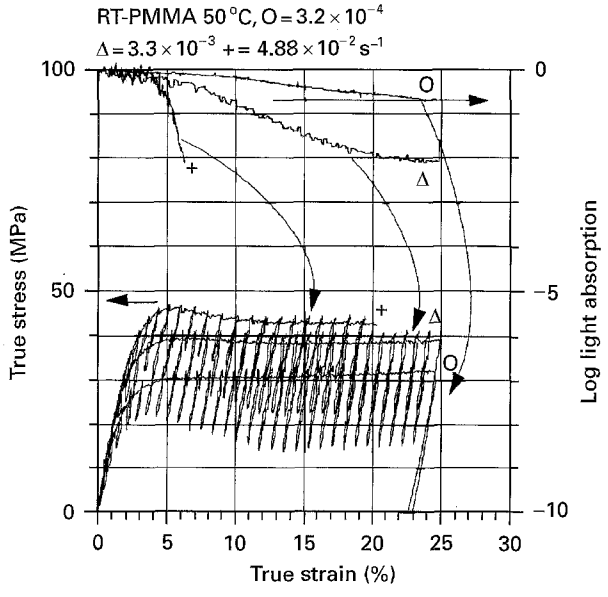

Figure 18 Light absorption and stress–strain curves at 50 °C and strain rates of 3.2×10^{-4}, 3.3×10^{-3}, and $4.9 \times 10^{-2}\ s^{-1}$. Values of the tensile modulus are, respectively, 1655, 1750 and 1788 MPa.

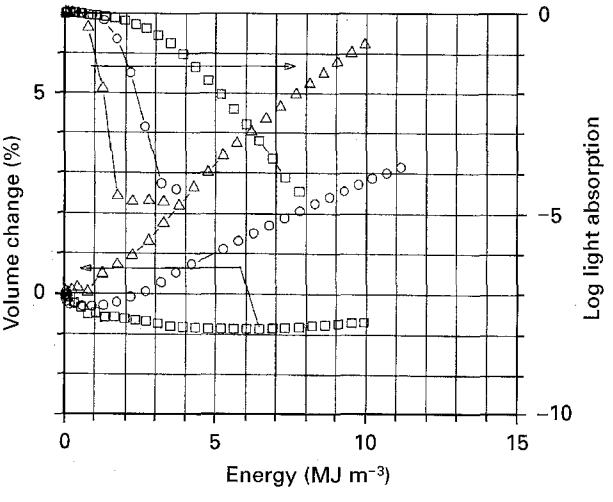

Figure 19 Volume change and light absorption as a function of the energy absorbed, at 20 °C and strain rates of (Δ) $3 \times 10^{-2}\ s^{-1}$, (○) $10^{-3}\ s^{-1}$ and (□) $5 \times 10^{-5}\ s^{-1}$.

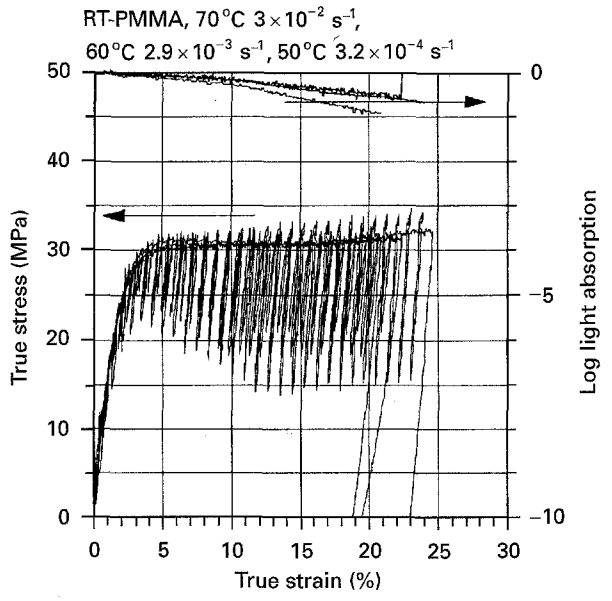

Figure 20 Stress–strain and light absorption curves at 70 °C and 3×10^{-2} s^{-1}, 60 °C and 2.9×10^{-3} s^{-1}, 50 °C and 3.2×10^{-4} s^{-1}. The tensile moduli are, respectively, 1390, 1580 and 1655 MPa.

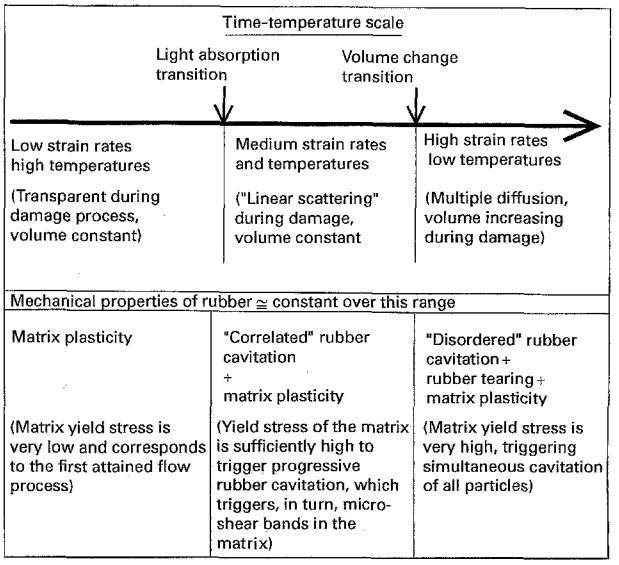

Figure 22 Relative position of light absorption and volume increase transitions on the time–temperature scale, together with the plausible micromechanisms of damage.

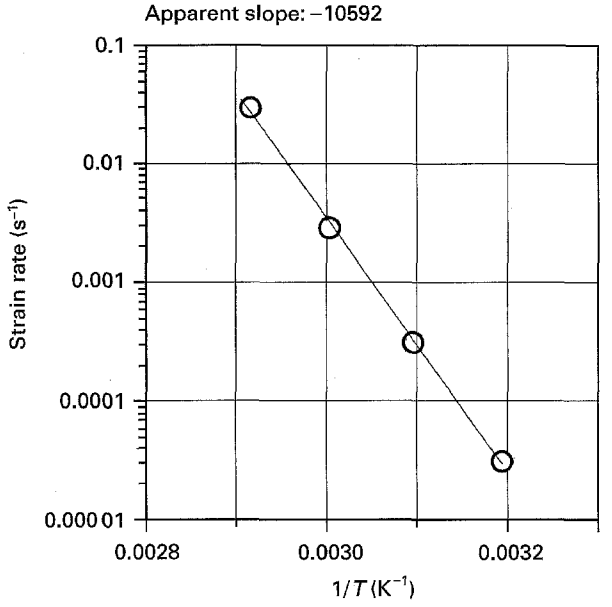

Figure 21 The Arrhenius plot for the start of light absorption at 40, 50, 60 and 70 °C. The slope corresponds to an apparent activation energy of 22 kcal mol^{-1}.

4. Discussion and conclusions: microscopic mechanisms

4.1. Particle cavitation versus matrix plasticity: experimental evidence

A number of general considerations of wide acceptance support the conclusions to be derived from the experiments reported in this paper. Firstly, volume change and light diffraction are related to particle cavitation in two very different ways. Volume changes at onset of particle cavitation are usually not detectable, a void measuring 10% of the particle diameter in each particle increasing the average volume by only 0.04% at 40% particle content, which is far below the experimental precision. Hence volume increase is an indicator not of the onset of cavitation, but rather of extensive rubber rupture and stretching in the particles. On the contrary, light diffraction is a reliable indicator of the onset of particle cavitation [17]. Secondly, at small strains where cavitation and plasticity begin to develop, the mechanical "contrast" between the rubber particles and the matrix is mainly a shear modulus contrast, the bulk moduli being somewhat similar. Therefore, only hydrostatic pressure exists within the particles during the deformation process before cavitation, whereas in the matrix, shear stresses are high around the particles. Microscopic damage then results from competition between shear yielding in the glassy matrix and cavitation in the rubber particles. In addition, both shear yielding in the matrix and cavitation in the rubber are inhibited below certain threshold levels of stress and energy density storage. Finally, it is important to recall that in the time and temperature range described in the present work, the matrix (PMMA) lies below its glass transition but near its secondary transition, the β peak, which governs solid-state plasticity. Thus, the yield stress of the matrix varies over the time and temperature range investigated. In the same range, the rubber of the particles lies far above its glass transition, with the result that the mechanical properties of the rubber remain almost constant with time and temperature over the range investigated, as do the threshold levels for rubber cavitation and rupture. Consequently, one might expect the "damage" thresholds of the matrix and the rubber to cross over in this range. Because light diffraction and volume changes exhibit separate transitions, three different types of behaviour are possible during the damage process, as outlined in Fig. 22.

Experimentally, three type of microstructural evolution may be distinguished during the deformation process.

(i) At very low strain rates or high temperatures, the volume remains constant and the material transparent, the absence of light diffusion indicating a lack of

cavitation in the rubber. Deformation of the material is then entirely due to plastic deformation of the matrix, as it is often the case in pure amorphous glassy polymers at high temperatures and low strain rates. However, pure PMMA would break at very low strain under the strain rate and temperature conditions of the present study. In RT-PMMA it is probable that each rubber particle induces micro-shear bands, which prevent a brittle rupture, and leaves the rubber particles deformed but undamaged. The mechanical "contrast" between the particles and the matrix seems to trigger local plasticity in the matrix around the particles. Hence the deformation process could be termed "plasticity" rather than damage, and is highly energy consuming, the low yield stress of the matrix under these conditions most likely being responsible for this behaviour.

(ii) At intermediate strain rates and temperatures, there is a rate–temperature range where light diffusion takes place during the damage process, in the absence of any volume change. Light diffusion indicates particle cavitation on organized sites along inclined bands, the "croids" [10], or dilatational bands [13]. As soon as a particle cavitates, a micro shear band propagates in the matrix around this particle, until it reaches another particle which cavitates in turn. The volume remains constant within the experimental detection limit of less than 1%. In fact, the holes in the rubber may be as small as 10 nm, which corresponds to 5% of the particle diameter, and leads to a volume change of only 5×10^{-5} if all particles cavitate [12, 14, 20].

The onset of cavitation takes place under time–temperature conditions for which the yield stress of the material reaches precisely 30 MPa. As described elsewhere [14], the creation of a void in rubber is subject to mechanisms with thresholds, related to the size of the void and its energy of formation. The precise level of the matrix yield stress below which cavitation does not exist, would therefore seem to reflect the thresholds to be overcome in order to create the cavity in the rubber.

In this intermediate range, the light diffraction pattern remains almost constant in shape but increases in intensity with increasing strain. Light absorption due to particle cavitation increases approximately linearly with strain (Fig. 20). Hence the number of cavitated particles must increase steadily with strain, the ruined particles being located along inclined lines as shown theoretically elsewhere [13] and experimentally in Fig. 10. The overall damage process could be described as "ordered", macroscopically homogeneous, triggering of progressive particle cavitation and micro-yielding in the matrix up to 20% strain. This process is still energy consuming, as deformation mainly arises from plasticity occurring in the matrix immediately after particle cavitation.

(iii) At high strain rates or low temperatures, although the onset of cavitation takes place as in the intermediate range, the number of cavitated particles and hence the light absorption increases sharply within a few per cent strain at quasi-constant volume (Figs 18 and 19). Localization of the cavitated particles on dilatational bands is visible on the diffraction pattern only in the very early stages before multiple light scattering occurs. The onset of macroscopic volume increase takes place at a low level of strain. Thus it would appear that cavitation is triggered quasi simultaneously in all particles and that the subsequent deformation is absorbed by extensive rubber deformation, rupture and fibrillation in the particles, which would explain the volume increase. The low activation energy for the volume increase (12 kcal mol^{-1}) further indicates a mechanism depending largely on properties of the rubber. At the highest strain rate shown in Fig. 14, the slope of the volume increase reaches 50% of the slope corresponding to a purely cavitational uniaxial deformation. Plasticity of the matrix is surely present at this stage of damage, but does not seem to play an important role, once again most likely on account of high yield stress of the matrix, which would lead to hydrostatic pressures far above the cavitation thresholds and thus to extensive rubber damage before matrix yielding. The high value of the damage, D, and the low energy consumption at high strain rates, are consistent with this type of micro-mechanism.

4.2. Threshold level yield stress

Our experiments indicate that the core–shell rubber particles cavitate when the yield stress reaches 30 MPa. An analysis of the stress, strain and energy states of an isolated pure rubber particle at the onset of cavitation has shown cavitation in the rubber to be governed by two equations [14]: the energy barrier, U_b, to initiate the void in the rubber

$$U_b = \frac{16\pi}{A^2} \frac{\Gamma_{st}^3}{\sigma_{h\,crit}^{\infty 2}} \tag{5}$$

and the critical equilibrium hydrostatic stress, $\sigma_{h\,crit}^{\infty}$, of the cavity

$$\sigma_{h\,crit}^{\infty} = \frac{2.6}{A} b_0^{-3/4} k_p^{1/4} \Gamma_{st}^{1/2} (\Gamma_F + \Gamma_{st})^{1/4} \tag{6}$$

where b_0 is the radius of the particle, Γ_F the rubber fracture energy ($\approx 0.05\ J\,m^{-2}$), Γ_{st} the rubber surface tension ($\approx 0.03\ J\,m^{-2}$).

$$A = \frac{(1 - \nu_m)}{(1 + \nu_m)} \frac{9k_p}{4\mu_m + 3k_p} \tag{7}$$

where $\mu_m \approx 1$ GPa, is the shear modulus of the matrix, and k_p is the homogenized bulk modulus of the rubber particle. These equations are only valid for small particles of pure rubber, typically less than 1 μm diameter, in the absence of interactions between particles. In the case of 200 nm pure rubber particles in PMMA, the calculated critical hydrostatic pressure in the rubber is 11.3 MPa, which corresponds to 34 MPa under uniaxial tension. This result is close to the measured value of 30 MPa, even though the experiments were performed on core–shell particles, and in the presence of particles interactions.

The energy storage is readily calculated for undamaged core–shell particles. When a cavity appears in the rubber shell, spherical symmetry is lost, and the

energy dissipated during cavity formation is not clearly defined. Nevertheless, because a cavity in the rubber shell will release the hydrostatic pressure as in a pure rubber particle [21], the same principles of calculation may be employed as for pure rubber [14]. If the method for pure rubber particles without particle interactions is applied to core–shell particles with interactions, three corrections should be made:

(i) the stored energy is overestimated as the bulk modulus of the core is higher than the bulk modulus of the rubber;

(ii) on the contrary, the greater surface area creation required for pressure release in the rubber shell, leads to an underestimation of the energy consumption;

(iii) interactions between particles are not taken into account, with a resultant overestimation of the threshold stress for cavitation.

Despite the neglect of all these unknown corrections, the calculated stress (34 MPa) leading to cavitation is as described above close to the measured value (30 MPa).

4.3. Stress and strain states in core–shell particles

As mentioned in this and many other papers, in the case of pure rubber particles, there are no shear stresses in the rubber and cavitation arises only from hydrostatic pressures. Using any standard finite element software it is easily shown that the same rule is valid for core–shell (hard core) particles provided the thickness of the rubber layer is at least a few per cent of the particle radius. At small strains, the rubber behaves like a "liquid" layer between the matrix and the core. As shown in Fig. 23, the core which is subjected only to hydrostatic pressure remains spherical, whereas the "hole" in the matrix becomes elliptical during the deformation process. On account of its very low shear modulus and high extension capacity, the rubber flows toward the poles until its limiting extension, λ_{max}, is attained somewhere in the shell. Shear strain hardening then appears in the rubber, and results in shear stresses. Appendix 2 gives details for calculation of the extension ratio of the rubber at the equator and poles (Fig. 24). The limiting extension ($\lambda_{max} \approx 5$) is reached at the equator at about 5% external strain, long before it is reached at the poles, at the usual rubber content of about 15%.

Because rubber cavitation is triggered by an energy criterion, a cavity may appear before or after the limiting extension is reached somewhere in the shell. Hence cavitation in the rubber shell may occur in two different situations.

(i) The threshold energy of cavitation [14, 20] is attained before the rubber reaches its critical extension. If the shear modulus of the rubber is neglected, stress in the rubber remains hydrostatic anywhere in the shell, despite its ellipsoidal deformation, as the rubber behaves like a liquid. However, as the shear modulus is not strictly zero, this ellipsoidal deformation leads to a small additional tension at the poles and a small additional compression at the equator

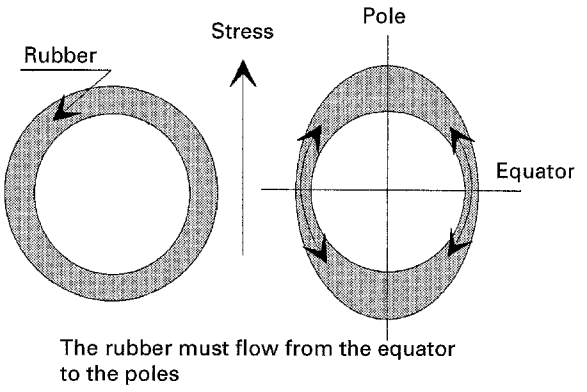

Figure 23 Deformation of the core relative to that of the hole in the matrix. The rubber flow from the equator to the poles stops when its limiting extension ratio is attained.

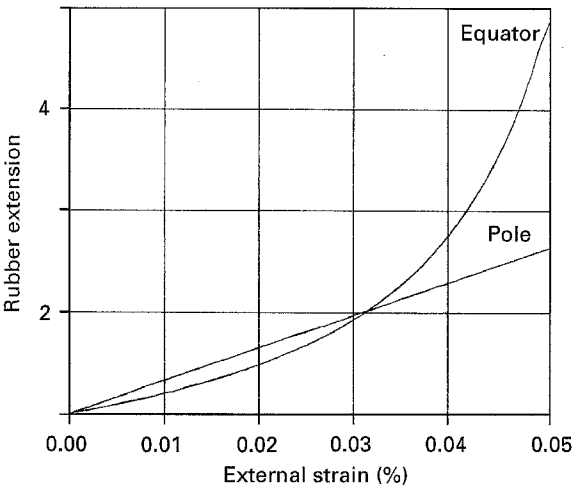

Figure 24 Rubber extension at the poles and equator of the particle as a function of external strain at 15% rubber content.

superimposed on the hydrostatic pressure. Although hydrostatic strain still constitutes the major part of the strain energy stored in the rubber and involved in the cavitation, the small supplementary tension probably initiates the damage process at the poles.

(ii) The critical extension is reached before the threshold energy of cavitation. Strong shear strain hardening then occurs at the equator, blocking the rubber flow towards the poles where the pressure is still hydrostatic and leading to high radial compression and lowering of the hydrostatic pressure at the equator. At the pole, the insufficient material flow results in an increase in hydrostatic pressure to attain rapidly the threshold energy for cavitation.

In both cases, cavitation occurs first at the poles.

4.4. Conclusions concerning the mechanism of damage

Fig. 25 illustrates the now generally accepted mechanism of damage for the case of pure rubber particles. The most relevant factor is the very low shear modulus of the rubber relative to that of the matrix, as opposed to the bulk modulus of the rubber which is of the same order of magnitude as that of the matrix.

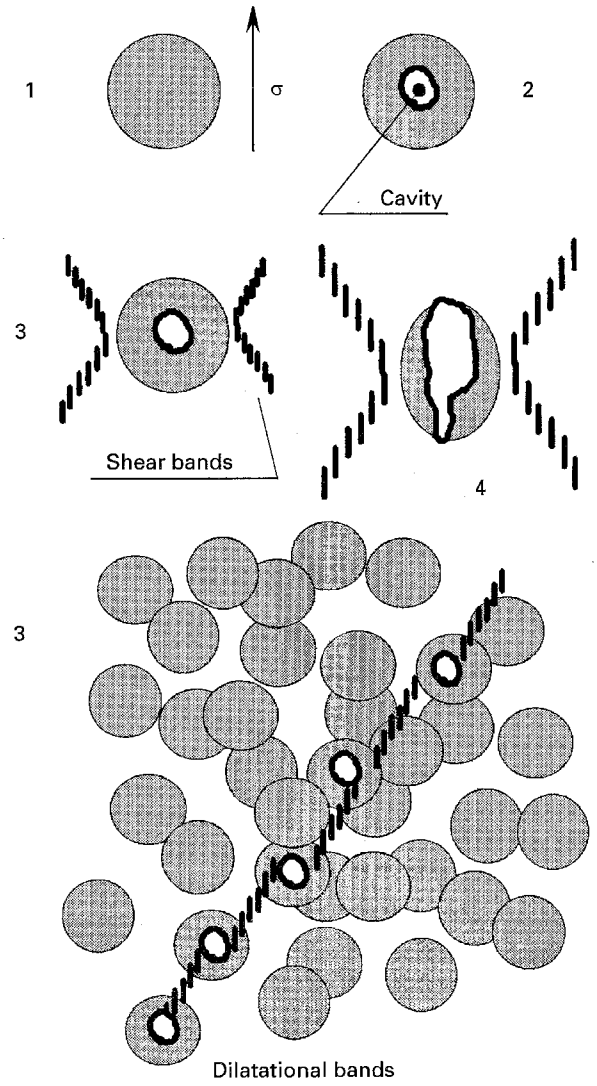

Figure 25 The generally accepted stepwise mechanism of damage in a matrix containing pure rubber particles. Steps 1 and 2: the external uniaxial stress produces triaxial stresses locally in the matrix, and hydrostatic stresses in the rubber, which results in rubber cavitation. Steps 2 and 3: high external uniaxial stress produces shear bands in the matrix. Hence cavitation takes place at correlated sites. Step 4: the external uniaxial flow produces shear plasticity in the matrix and tearing in the rubber.

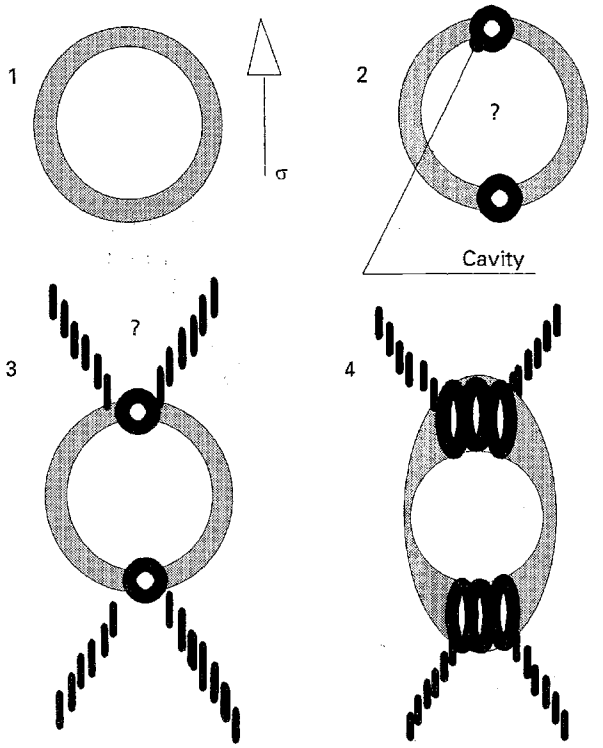

Figure 26 Hypothetical stepwise mechanisms of damage in a matrix containing core–shell particles. Steps 1 and 2: the external uniaxial strain produces triaxial stresses in the matrix and hydrostatic pressure in the rubber and core of the particles. Cavitation occurs at the poles in the rubber shell. Steps 2 and 3: high external uniaxial high strain produces high shear in the matrix. No stress remains in the rubber of the cavitated particle and cavitation takes place at correlated sites as in the case of pure rubber particles. Step 4: the external uniaxial flow produces shear plasticity in the matrix and in the rubber tensile stretch at the poles and compression at the equator. Shear stress may not be entirely absent from the shell.

Hence no significant shear stress is transmitted from the bulk matrix to the particles, and almost pure hydrostatic pressure ($\approx \sigma/4$ under uniaxial tension) dominates in the rubber. A rubber particle may then cavitate, lowering the inner hydrostatic pressure to nearly zero and inducing a micro-shear band in the surrounding matrix. This shear band may, in turn, trigger cavitation in a neighbouring particle. As a result, the cavitated particles are located at particular sites in the material, leading to a cross-shaped light scattering pattern.

The case of particles with hard core and rubber shell is presented in Fig. 26. Finite element calculations show that a shell of only a few per cent relative thickness prevents the transmission of shear stresses to the core. The core then remains spherical during ellipsoidal deformation of the rubber shell and cavitation may be expected to occur at the poles of the shell. Despite a much lower rubber content, the overall mechanism could well remain the same as in the case of pure rubber particles.

This type of micro-mechanism readily accounts for the brittleness of the material at high strain rates. In the presence of two competing processes (cavitation in the rubber and shear yielding in the matrix at low strain rates), the low yield stress of the matrix leads to shear yielding immediately after or even before cavitation, whereas at high strain rates the high yield stress of the matrix results in extensive rubber cavitation and rupture before the onset of shear yielding. Damage in the rubber being considerably less energy consuming than yielding in the glassy matrix, high strain rates are characterized by brittle behaviour.

Appendix 1. Light absorption by damaged particles

The particle properties are N the number of particles per unit volume, v_p the particle volume fraction, d the particle diameter (including the rubber shell), and $\langle\Delta\rangle$ the mean distance between particles.

Assuming nothing about the location of the particles in the matrix on a more or less regular lattice, for simple dimensional reasons, these properties are

connected in the following way

$$(d/\langle\Delta\rangle)^3 \approx v_p \quad \text{(A1)}$$

$$N d^3 \approx v_p \quad \text{(A2)}$$

Fig. A1 shows the principles of the optical measurement system. When ruined, a particle becomes light scattering or at least produces a light deflection if the optical index has changed. As the light beam is filtered by a lens combined with a pin hole, scattered or deflected beams do not reach the detector. The extinction ratio corresponds to the square of the ratio between the pin hole diameter and the lens focus length (about 10^{-4}), and the experimental system is similar to phase contrast visualization. Total extinction is calculated as the integral over the sample thickness, T, of the extinction due to an elementary layer of thickness, dT.

The ruined particle properties are N_d the number of ruined (scattering) particles per unit volume, $\phi = N_d/N$ the ruined particle fraction (in number), dS the scattering cross-section of a ruined particle, and $\xi = dS/d^2$ the ruined particle "opacity" (≤ 1).

In a layer of thickness $\langle\Delta\rangle$ and cross-section 1, the properties are as follows. The number of ruined particles is $\langle\Delta\rangle N_d$. The total scattering section of the layer is given by

$$\begin{aligned} \Delta S &= N_d\langle\Delta\rangle dS \\ &= N\,\phi\langle\Delta\rangle dS \\ &= v_p^{2/3}\,\phi\xi \end{aligned} \quad \text{(A3)}$$

The light intensity change is

$$\delta(I_{out}/I_{in}) = 1 - v_p^{2/3}\phi\xi \quad \text{(A4)}$$

After crossing m layers $\langle\Delta\rangle$, the light intensity change is

$$I_{out}/I_{in} = (1 - v_p^{2/3}\,\phi\xi)^m \quad \text{(A5)}$$

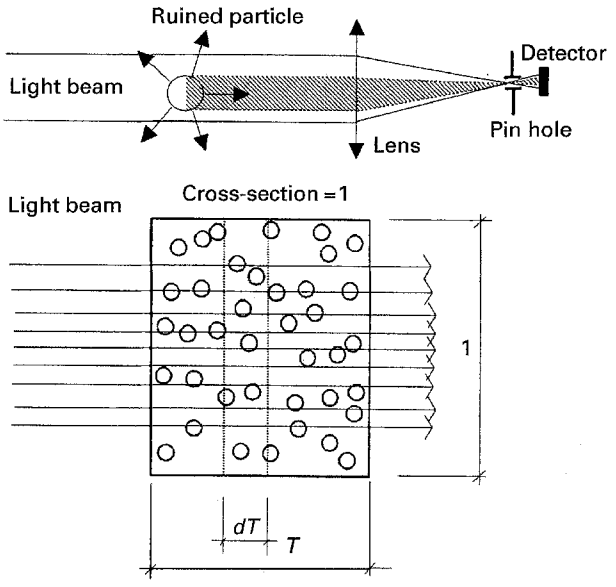

Figure A1 Principles of the optical measurement system: a ruined particle becomes light scattering and beam filtering suppresses this scattered light at the detector. The system is similar to phase-contrast visualisation.

The number of layers m is simply

$$m = T/\langle\Delta\rangle = T\,v_p^{1/3}\,d^{-1} \quad \text{(A6)}$$

Finally, the transmitted light intensity is

$$\log(I/I_0) = T\,v_p^{1/3}\,d^{-1}\log(1 - \phi\xi\,v_p^{2/3}) \quad \text{(A7)}$$

This equation shows that it is not possible to distinguish the ratio of ruined particles, ϕ, and the particle opacity, ξ. In the case of RT-PMMA, where the usual values are $v_p = 0.4$, $d = 2\times10^{-7}$, $T = 0.002$ and $\langle\Delta\rangle \approx 2.7\times10^{-7}$, strong damage leads to almost zero light transmission ($I/I_0 = 10^{-5}$) and hence to a $\phi\xi$ value of 2.8×10^{-3}! When the light transmission falls to zero, only a very small number of particles is ruined.

As $\phi\xi$ is small

$$\log(1 - \phi\xi\,v_p^{2/3}) \approx -\phi\xi\,v_p^{2/3}\log(e) \quad \text{(A8)}$$

giving the simple equations

$$\log(I/I_0) \approx -0.43T\,v_p\,\phi\xi\,d^{-1} \quad \text{(A9)}$$

or

$$\phi\xi \approx -d(0.43T\,v_p)^{-1}\log(I/I_0) \quad \text{(A10)}$$

and for the standard sample in this paper

$$\phi\xi \approx -0.58\times10^{-3}\log(I/I_0) \quad \text{(A11)}$$

At high damage values, still only 1 in 1000 particles is ruined and the mean distance between ruined particles is only ten times ($1000^{1/3}$) larger than the mean inter-particle distance. Because $\langle\Delta\rangle \approx 2.7\times10^{-7}$, the mean distance between ruined particles, $\langle\Delta_r\rangle$, is about 2.7×10^{-6} (2.7 μm). However, as the ruined particles are known from the light scattering pattern to be located at correlated sites in the damaged material, this mean distance must be considered with care. Owing to correlation between ruined particles, the scattering cross-section may be larger than one single particle, and the number of ruined "sites" lower than ϕ.

Appendix 2. Stresses and strains around core–shell particles

Fig. A2 shows representations of the initial and deformed particles. All the following calculations apply to an isolated particle, in the absence of particle interactions and are given in detail elsewhere [14].

The particle geometry is v_r the volume fraction of rubber in the particle, ρ_c the radius of the core, ρ_s the radius of the shell, and e the thickness of the rubber shell.

In the undeformed state, the following relations holds

$$1 - v_r = \left(\frac{\rho_c}{\rho_s}\right)^3 \quad \text{(A12)}$$

$$e = \rho_s - \rho_c. \quad \text{(A13)}$$

The material properties are ε^∞ the mean external uniaxial strain, E_m Young's modulus of the matrix, E_t Young's modulus of the whole material, ν_m Poisson's ratio of the matrix, μ_m shear modulus of the matrix, k_c the bulk modulus of the particle core, k_s the

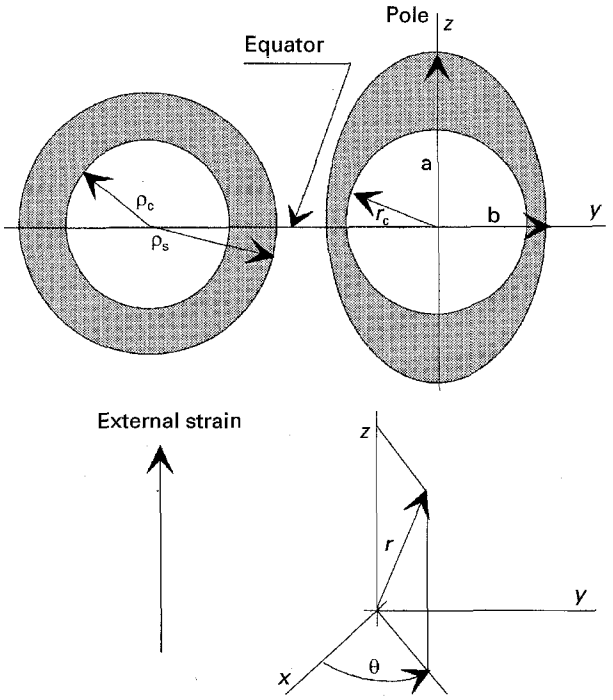

Figure A2 Ellipsoidal deformation of a core–shell (hard core) particle under uniaxial tension. At low strains, the core remains spherical.

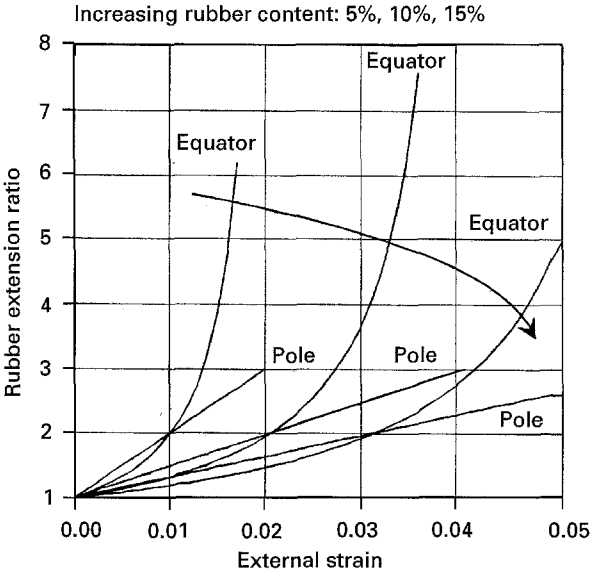

Figure A3 Extension ratios in the rubber at the pole $\lambda_{r\text{-pole}}$ and equator ($\lambda_{z\text{-equa}} = (\lambda_{\theta\text{-equal}}\,\lambda_{r\text{-equa}})^{-1}$) versus external strain for 5%, 10%, 15% rubber content in the particle.

bulk modulus of the rubber shell, k_p the homogenized bulk modulus of the particle, and σ_h^∞ the hydrostatic component of the external stress with

$$k_p = \frac{k_c k_s}{k_s(1-v_r) + k_c v_r} \tag{A14}$$

$$\sigma_h^\infty = \frac{E_t \varepsilon^\infty}{3} \tag{A15}$$

In the deformed state, the hydrostatic stress in the shell and core is

$$\sigma_h = \frac{(1-\nu_m)}{(1+\nu_m)}\frac{9k_p\sigma_h^\infty}{4\mu_m + 3k_p} = \frac{(1-\nu_m)}{(1+\nu_m)}\frac{3k_pE_t\varepsilon^\infty}{4\mu_m + 3k_p} \tag{A16}$$

and the radius of the core is

$$r_c = \rho_s(1-v_r)^{1/3}(1 + C\varepsilon^\infty) \tag{A17}$$

where

$$C = \frac{(1-\nu_m)\,E_m k_p}{(1+\nu_m)k_c(4\mu_m + 3k_p)} \tag{A18}$$

The external part of the shell is an ellipsoid of axes a and b [21, 22]

$$a = \rho_s[1 + \varepsilon^\infty(A - P)] \tag{A19}$$

$$b = \rho_s[1 + \varepsilon^\infty(B - P)] \tag{A20}$$

where

$$A = \frac{3(1-\nu_m)(9 + 5\nu_m)}{2(7 - 5\nu_m)} \tag{A21}$$

$$B = \frac{3(1-\nu_m)(-1 - 5\nu_m)}{2(7 - 5\nu_m)} \tag{A22}$$

$$P = \frac{3(1-\nu_m)k_p}{8\mu_m + 6k_p} \tag{A23}$$

The extension ratio along the r-axis at the equator, λ_{equa}, and the pole, λ_{pole}, of the particle are deduced from

$$\lambda_{r\text{-equa}} = \frac{b - r_c}{e} = \frac{1-(1-v_r)^{1/3} + \varepsilon^\infty[B - P - C(1-v_r)^{1/3}]}{1-(1-v_r)^{1/3}} \tag{A24}$$

$$\lambda_{r\text{-pole}} = \frac{a - r_c}{e} = \frac{1-(1-v_r)^{1/3} + \varepsilon^\infty[A - P - C(1-v_r)^{1/3}]}{1-(1-v_r)^{1/3}} \tag{A25}$$

Along the z-axis, the extension at the equator is

$$\lambda_{z\text{-equa}} = \frac{b}{\rho_s} = 1 + \varepsilon^\infty\,[B - P - C(1-v_r)^{1/3}] \tag{A26}$$

Assuming the rubber volume to remain constant, at the equator one has

$$\lambda_{\theta\text{-equa}}\,\lambda_{r\text{-equa}}\,\lambda_{z\text{-equa}} = 1 \tag{A27}$$

$$\lambda_{\theta\text{-equa}} = \frac{1-(1-v_r)^{1/3}}{\{1-(1-v_r)^{1/3} + \varepsilon^\infty[B - P - C(1-v_r)^{1/3}][1 + \varepsilon^\infty(B - P - C(1-v_r)^{1/3})]\}} \tag{A28}$$

Fig. A3 shows that the extension ratio increases rapidly at the equator even at low external strain.

References

1. C. B. BUCKNALL, I. K. PARTRIDGE and M. V. WARD, *J. Mater. Sci.* **19** (1984) 2064.
2. NILESH SHAH, *ibid.* **23** (1988) 3623.
3. C. WROTECKI, P. HEIM and P. GAILLARD, *Polym. Eng. Sci.* **31** (1991) 213.
4. P. HEIM, C. WROTECKI and P. GAILLARD, *Polymer* **34** (1993) 1653.
5. D. S. PARKER, H. J. SUE, J. HUANG and A. F. YEE, *ibid.* **31** (1990) 2267.
6. Y. OKAMOTO, H. MIYAGI and S. MITSUI, *Macromolecules* **26** (1993) 6547.
7. R. J. GAYMANS, R. J. M. BORGGREVE and A. J. OOSTENBRINK, *Macromol. Chem. Macromol. Symp.* **38** (1990) 125.
8. R. A. BUBECK, D. J. BUCKLEY, E. J. KRAMER and H. R. BROWN, *J. Mater. Sci.* **26** (1991) 6249.
9. P. A. LOVELL, A. J. RYAN, M. N. SHERRETT and R. J. YOUNG, in Proceedings of "Deformation, Yield and Fracture of Polymers", Cambridge 1994, (The Institute of Materials, London 1994).
10. H. Y. SUE, *J. Mater. Sci.* **27** (1992) 3098.
11. C. B. BUCKNALL, C. A. CORREA, V. L. P. SOARES and X. C. ZHANG, in Proceedings of "Deformation, Yield and Fracture of Polymers", Cambridge 1994, (The Institute of Materials, London 1994).
12. C. B. BUCKNALL, A. KARDOPINIS and X. C. ZHANG, *J. Mater. Sci.* **29** (1994) 3377.
13. A. LAZZERI and C. B. BUCKNALL, *ibid.* **28** (1993) 6799.
14. C. FOND and R. SCHIRRER, *Int. J. Fracture* **77** (1996) 141.
16. O. FRANK and J. LEHMANN, *Coll. Polym. Sci.* **264** (1986) 473.
17. D. DOMPAS, G. GROENINCKX, M. ISOGAWA, T. HASEGAWA and M. KADOKURA, *Polymer* **35** (1994) 4750.
18. K. DIJKSTRA, A. VAN DER WAL and R. J. GAYMANS, *J. Mater. Sci.* **29** (1994) 3489.
19. A. BREUER, F. HAAF and J. STABENOW, *J. Macromol. Sci. Phys.* **B14** (1977) 387.
20. D. DOMPAS and G. GROENINCKX, *Polymer* **35** (1994) 4743.
21. J. D. ESHELBY, *Proc. R. Soc. Lond. A* **241** (1957) 376.
22. *Idem, ibid.* **252** (1959) 561.

Received 8 January
and accepted 2 July 1996